Hindawi
International Journal of Photoenergy
Volume 2023, Article ID 8505609, 21 pages
https://doi.org/10.1155/2023/8505609

Research Article

Comparative Analysis of Different Control Strategies for Relift Luo Converter

R. Banupriya,[1] R. Nagarajan,[2] and K. R. N. Kalis[3]

[1]*Department of Electrical and Electronics Engineering, PGP College of Engineering and Technology, Tamil Nadu, India*
[2]*Department of Electrical and Electronics Engineering, Gnanamani College of Technology, Tamil Nadu, India*
[3]*Department of Electronics and Communication Engineering, Kongunadu College of Engineering and Technology, Tamil Nadu, India*

Correspondence should be addressed to R. Nagarajan; krnaga71@yahoo.com

Received 21 March 2023; Revised 19 September 2023; Accepted 29 September 2023; Published 14 October 2023

Academic Editor: Fayaz Hussain

Dual-output DC to DC converters have drawn attention in the domestic, automobile, and industrial domains. A dual-output converter usually provides a voltage step-down channel and a voltage step-up channel. Typically, an automobile needs a battery charging unit, a traction motor drive, and several other applications. A typical application may require two channels of DC output with a low-voltage (LV) channel and a high-voltage (HV) channel. While the generic boost-derived and quadratic boost-derived dual-output converters are available in the literature, this article focuses on the control aspects of a relift type Luo converter-derived dual-output converter (LDDOC). A solar photovoltaic (SPV) source is the main power, and it charges a battery. The LV loads may be connected across the battery, and the relift stage delivers a regulated 48 V output. The regulation of the 48 V output using a PI controller, a fuzzy logic controller, an ANN-based controller, and a sliding mode controller (SMC) has been studied using simulations. The simulations reveal that the sliding mode controller is advantageous because of meeting out the required performance, easy implementation, and low cost. An experimental setup has also been developed to verify the performance of the sliding mode controller for the regulation of the HV channel output voltage at 48 V.

1. Introduction

When a single DC voltage source is available and if it is necessary to derive two DC voltage outputs, then the dual-output DC to DC converter is used. The two outputs may be of equal voltage and isolated, nonequal and isolated, nonisolated but equal, or nonequal and isolated, and in all these cases, we use different topologies to suit the exact requirement. If two voltages are to be derived from a single DC source and if one of the two voltages is required to be less than the source voltage and the other one is required to be greater than the source voltage, we need to have a buck channel and a boost channel. Such topologies are usually called as the dual-output converter, and based on the core converter topology used in the system, they are called as the generic boost-derived dual-output converter, the quadratic boost-derived dual-output converter, and so on. In this work, the relift Luo converter is used as the basic boost converter and an additional bidirectional buck boost system is incorporated. The relift Luo converter forms the main HV channel, and the attached bidirectional buck boost arrangement is used to include a battery and an LV channel. The source of external power is derived from a standard DC voltage source.

Down in the literature, certain topological variants of multioutput DC to DC converters have been reported. Some of the milestone works have been outlined here so as to consider the merits and demerits of the existing systems. The authors in [1] have developed a multiport DC to DC converter that offers high-voltage gain in the HV channel, and it has been demonstrated how a solar photovoltaic-powered battery charging subsystem could be incorporated. In reference [2], a DC to DC converter with high-power conversion efficiency over a wide range of operation has been presented. The work exhibits the design of a zero voltage switching (ZVS). A bidirectional DC to DC converter has been proposed and validated by the authors in [3]. In a similar development, the authors in [4]

have developed a hybrid energy-sourced DC to DC converter featuring soft switching and nonisolation between the ports. Quasiresonant DC to DC converters with improved power conversion efficiency based on ZVS have been presented by the authors in [5, 6].

Since the power electronic switches operate in discretely switched fashion, the authors in [7] have shown that the interleaved converters are useful in increasing the utility of the sources. Transformers and inductors play important role in the design and development of isolated and nonisolated high-voltage gain DC to DC converters, and such a topology has been put forward by the authors in [8]. Multiport topologies are developed with the standard DC to DC converter as the core converter and adding some subcircuits to the core converter [9]. Such configurations have been built using the SEPIC [10] and the CUK converters as well [11].

Many researchers have relied upon the solar photovoltaic source and multiport configurations with provision for battery charging [12]. Deriving power from the solar photovoltaic source for charging batteries has been proposed and validated by the authors in [13]. Multiport topologies with provision to include solar PV source suitable for water pumping scheme have been forwarded by the authors in [14]. As for the control schemes, the conventional PI controllers have been predominant [15]. Also, many authors have demonstrated the use of soft computing techniques for the purpose of maximum power point tracking applicable for renewable energy source-based systems [16].

Integration of hybrid energy sources and catering for linear and nonlinear loads has been focused by the authors in [17]. A comprehensive review of the power electronic converters applicable for solar photovoltaic power harvesting has been carried out by the authors in [18]. In a further development, the authors in [19] have developed a solar photovoltaic simulator for the purpose of carrying out research activities.

Thus, the major observation is that multiport DC to DC converters have been researched extensively, particularly with a focus on the integration of solar photovoltaic source to the microgrid wherein battery-based storage facilities are also included. In [20], a cascaded DC to DC converter unit for application in a microgrid has been proposed and validated, and the proposed scheme has exhibited a reduction of harmonics. A variety of multiport DC to DC converters have been presented by the authors in the article [21], and a Cuk-derived quadratic boost converter is demonstrated by the authors in [22]. In a similar development, a multiport DC to DC converter with the quadratic boost converter as the core converter and an SLL-based converter have been proposed and validated by the authors in [23, 24].

The authors in [25] have presented a combination of a superlift Luo converter with an additional buck feature, and in [26], a multiple output DC to DC converter has been presented. Further, in [27], a combination of the superlift Luo converter and the Cuk converter has been promoted. An interleaved DC to DC converter with single input and multiple outputs has been presented in [28]. Further, in [29], a dual-input dual-output converter suitable for electrical vehicle applications has been presented. Similarly, a hybrid PV and fuel cell inputs and dual-output converter have been demonstrated in [30].

The main observation from the existing literature is that wherever very high-voltage gain is required, the common choice is to use a transformer-based resonant DC to DC converter. Such configurations become heavy and costly, and they also suffer the nonlinearities caused by magnetic saturation effects. The idea of the resonant converter is impressive, but it suffers the bottleneck of the circuit deviating from resonant condition when the components degrade due to ageing or other adverse conditions. A more flexible high-voltage gain DC to DC converter is desirable for long-term operations.

Therefore, in this work, the relift Luo converter is considered as the core converter for a multiport DC to DC converter. In this article, the topology of the proposed dual-output converter with a HV and an LV channel is presented. The topological structures of the superlift and relift converters make it easier that an output voltage can be derived from each stage, and the topology yields itself for multiple outputs even with a single power electronic switch. This advantage of the relift converter is exploited in this work. The modes of operation are discussed with the step-by-step derivation of the average state space model for each and every subsystem of the complete work.

The organization of the article is as follows. A brief introduction is discussed in Section 1. The topology of the proposes dual-output converter system is discussed in Section 2. The solar PV energy harvesting and MPPT (Maximum Power Point Tracking) controller are discussed in Section 3. The mathematical and the circuit models developed in the MATLAB Simulink environment are presented in Section 4. The details of the experimental prototype and the results obtained are presented in Section 5. The article closes with a concluding note and a set of references.

2. Proposed Relift Luo Converter

The block diagram of the proposed system is shown in Figure 1. It consists of a two-stage relift converter, and a synchronous buck boost converter is introduced in between the two stages of the relift converter. The synchronous buck boost converter is a bidirectional converter used for charging the battery. The external input is supplied by a solar photovoltaic (SPV) panel, and the typical voltage range of the SPV source is 15 V to 25V. The SPV source drives the HV load and charges the battery as well. When the external voltage source is not available, the battery delivers power to the HV channel and gets discharged. In the common point between the first and second stages of the relift Luo converter, the battery control buck boost converter is connected.

2.1. Topology of the Relift Luo Converter. The topology of the proposed system is shown in Figure 2. The core converter is the relift Luo converter which can be treated as a set of two simple lift converters. A lift circuit generally comprises of a parallel charge circuit drawing current from the source and a series discharge circuit that delivers power to the load at a higher voltage level across the load or across the input port of the next stage of the series of cascaded converters. The parallel charge circuit and the series discharge circuit are formed by an inductor L and a capacitor C. These inductors

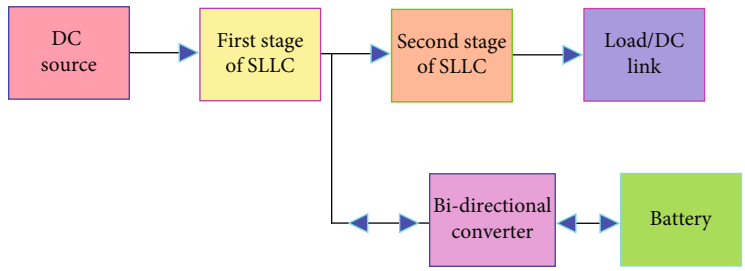

Figure 1: Block diagram of the proposed relift Luo converter.

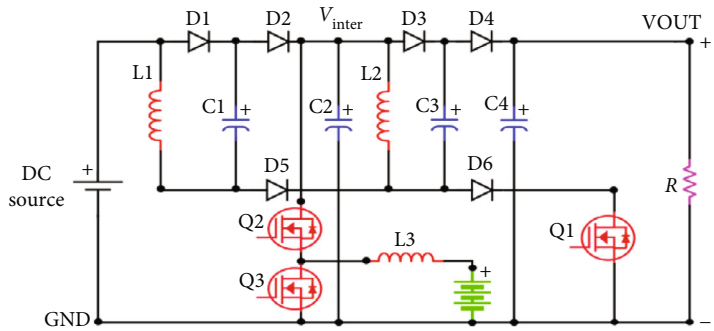

Figure 2: Topology for proposed relift Luo converter.

and capacitors are named L1 and C1 and L2 and C3 with capacitors C2 and C4 as the filter after the first and second stages. The lift converter uses a single power electronic switch Q1. Two additional switches Q2 and Q3 are used in the buck boost converter in the battery section. L3 is the boost inductor used in the battery charge discharge circuit.

The overall structure of the proposed system can be considered as three sections: the first lift section, the synchronous buck boost section, and the second lift section. Capacitor C2 is a filter capacitor for stage 1, and capacitor C4 is the ripple filter for the second stage. The voltage gain of the front end lift converter is given as

$$\frac{V_{out}}{V_{in}} = \frac{2-k}{1-k}. \tag{1}$$

In equation (1), k is the duty cycle applied at Q1. Similarly, the voltage gain of the second stage is also given as equation. The overall voltage gain of the relift Luo converter is given as

$$\frac{V_{out}}{V_{in}} = \left(\frac{2-k}{1-k}\right)^2. \tag{2}$$

If the duty cycle is 0.5, voltage gain of the relift converter is 9. If the input voltage is 12 V, then the output voltage will be 108 V. However, because of the voltage drops occurring in the diodes and the other passive components, the voltage gain is reduced. From the plot of the duty cycle versus V_{out} curve for the relift Luo converter, it has been observed that an output voltage of 72 V was obtained for a duty cycle of 0.5 while the input voltage is 12 V. This accounts to a practical voltage gain of 6 against the theoretical voltage gain of 9 for a duty cycle 0.5. The maximum voltage gain was found to occur for a duty cycle of 0.65.

In order to get an insight into the transient and steady-state behavior of the proposed system, the state space model of the system has been developed and it is simulated in the MATLAB Simulink environment. The proposed system can be treated as a set of three parts comprising of the source side lift stage of the relift Luo converter at the front end, the buck boost part at the middle, and the second or the load side part of the relift converter. The input voltage to the front end lift stage is denoted as V_{in}, the final output voltage is denoted as V_{out}, and the intermediate voltage after the first lift stage is denoted as V_{inter}. The buck boost section comprising the battery is connected across the capacitor C2, where the voltage is V_{inter}. The state model of the source side or front end lift stage and the final or the load side lift stage is similar. The switch Q1 is common for both the front end and load side lift stages. The state space model for front end lift stage is described herein.

By the principle of the relift converter, the switch Q1 is used by the source side and the load side lift stages in a simultaneous manner. For the purpose of analysis, a resistive load of 10 ohms has been considered. The two switching modes are shown in Figure 3. With respect to Figure 3(a), the lift stage consists of an input voltage of V_{in}, the load R, the power electronic switch Q1, and the diodes D1 and D2. Further, the components L1 and C1 form the parallel charge and series discharge circuit. C2 is the smoothing across the load resistor. There are three storage elements, and hence, three state variables are considered. The state equations can be derived using the fundamental principles and Kirchhoff's voltage and current laws for the two modes of the circuit formed by the switching states of Q1, as shown in Figures 3(b) and 3(c).

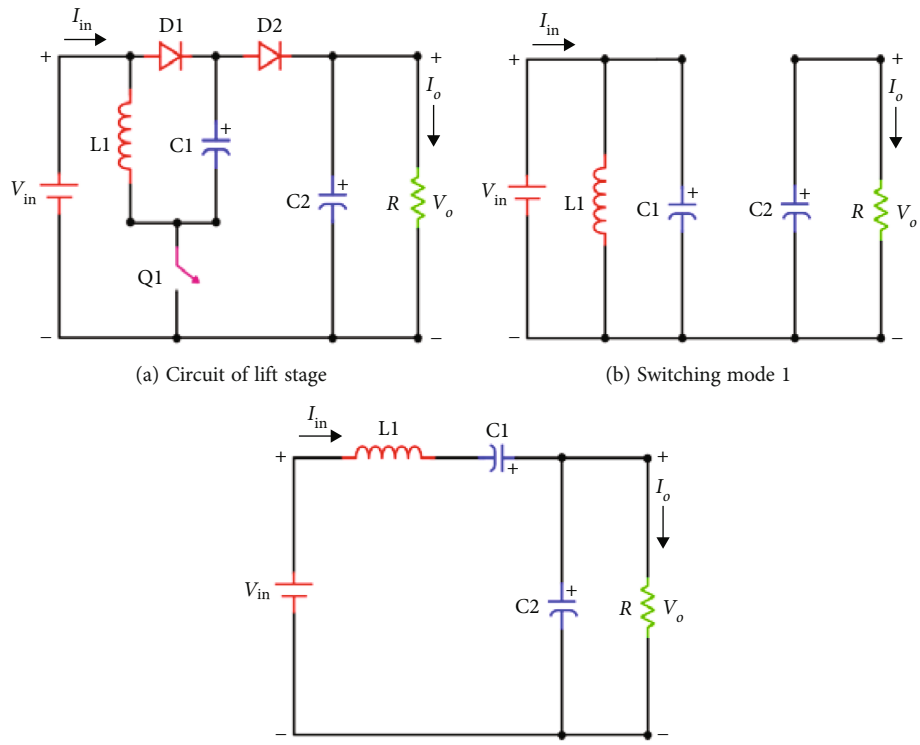

(a) Circuit of lift stage

(b) Switching mode 1

(c) Switching mode 2

Figure 3: Circuit of lift stage and switching modes.

The averaged state space model for the front end lift stage is shown in

$$\begin{bmatrix} \frac{diL1}{dt} \\ \frac{dvC1}{dt} \\ \frac{dvC2}{dt} \end{bmatrix} = \begin{bmatrix} \frac{1}{R_{in}L1} & \frac{d-1}{L1} & \frac{d-1}{L1} \\ \frac{1-2d}{C1} & \frac{-d}{R_{in}C1} & 0 \\ \frac{1-d}{C2} & 0 & \frac{-1}{RC2} \end{bmatrix} * \begin{bmatrix} iL1 \\ vC1 \\ vC2 \end{bmatrix} + \begin{bmatrix} \frac{1}{L1} \\ \frac{d}{R_{in}C1} \\ \frac{iL1}{C2} \end{bmatrix} * [V_{in}]. \tag{3}$$

In the state equation (3), the duty cycle applied to Q1 is denoted as d. The source resistance is R_{in}, and it is relatively very small. Inductor L1 = 1 mH and capacitor C1 = 250 microfarad and C2 = 6600 microfarad. In the similar manner, the state model of the second lift section which starts from capacitor C2 and terminated across the load of 24 or 48 ohms can be developed, and it is shown in

$$\begin{bmatrix} \frac{diL2}{dt} \\ \frac{dvC3}{dt} \\ \frac{dvC4}{dt} \end{bmatrix} = \begin{bmatrix} \frac{1}{R_{in}L2} & \frac{d-1}{L2} & \frac{d-1}{L2} \\ \frac{1-2d}{C3} & \frac{-d}{R_{in}C3} & 0 \\ \frac{1-d}{C4} & 0 & \frac{-1}{RC4} \end{bmatrix} * \begin{bmatrix} iL2 \\ vC3 \\ vC4 \end{bmatrix} + \begin{bmatrix} \frac{1}{L2} \\ \frac{d}{R_{in}C3} \\ \frac{iL2}{C4} \end{bmatrix} * [V_{in}]. \tag{4}$$

The component values for the first and second stages are identical. As for equation (4), the input voltage V_{in} is actually the voltage that appears across the intermediate DC link capacitor C2 after the first stage. The battery subsystem uses a synchronous buck boost converter. The buck section is built using the switch Q2 as the power control switch in the battery charge mode and Q3, while in the off state, as the freewheeling device. In the battery discharge mode, Q3 is the boost switch and Q2 is in the off state and serves as the reverse blocking diode. The voltage V_{inter} is the intermediate voltage across the capacitor C2, and it is actually the DC bus bar where the battery side synchronous buck boost converter is used. There are four different voltages of interest. The first is the SPV terminal voltage, which is represented by V_{in}, the second is the intermediate DC link voltage across C2, which is represented by the symbol V_{inter}, the battery voltage shown by the third one is $V_{battery}$, and the fourth is the load side voltage, which is indicated by the symbol V_{out}. The nominal voltages are $V_{in} = 12$ V to 17 V, $V_{inter} = 4$ V, $V_{battery} = 12$ V, and $V_{out} = 48$ V.

When the SPV source is available, the output voltage of 48 V is supplied to the load and the remaining power is used for charging the battery. When the 48 V load is not required to be operated, the SPV source is completely used for charging the battery. When the SPV source is not available, the battery supplies power to the 48 V load. The output voltage of 48 V is regulated using a closed loop controller. Figure 4(a) shows the buck switching modes, and Figure 4(b) shows boost switching mode operation of the system. The performance of a PI controller, a fuzzy logic controller (FLC), an artificial neural network (ANN), and a sliding mode controller (SMC) has all been compared based on dynamic simulations carried out in MATLAB Simulink.

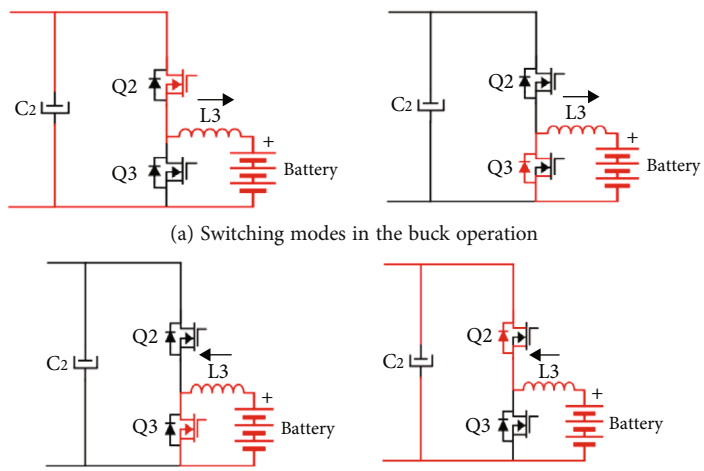

(a) Switching modes in the buck operation

(b) Switching modes in the boost operation

Figure 4: Buck and boost switching mode operations.

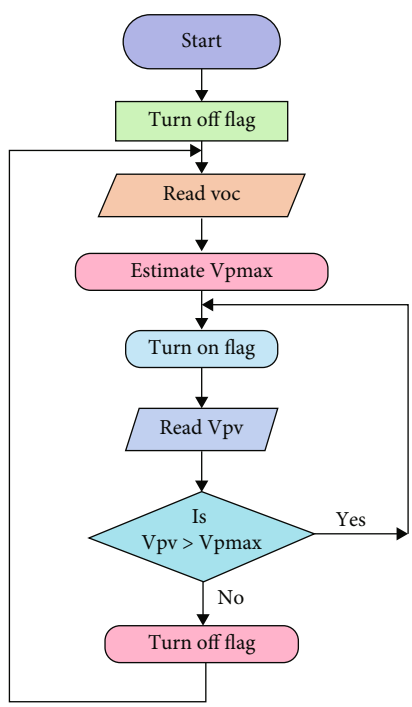

Figure 5: Flow chart of the SMC-based MPPT.

The voltage gain of the buck converter is given by

$$\frac{V_{\text{out}}}{V_{\text{in}}} = d. \tag{5}$$

The voltage gain of the generic boost converter is given by

$$\frac{V_{\text{out}}}{V_{\text{in}}} = \frac{d}{1-d}. \tag{6}$$

Table 1: Specifications of the proposed system.

Main source	SPV voltage source
Power rating of main source	15-25 V, 125 W*2 = 250 W
Voltage across the intermediate stage (LV)	24 V
Voltage across the HV channel output (HV)	48 V
Battery	12 V and 35 Ah
HV load	48 V, 24 ohms, and 96 W

Table 2: Modes of operations.

Mode	External source	Battery state	HV load
Mode 1	Available	Charging	Load on
Mode 2	Not available	Discharging	Load on
Mode 3	Available	Charging	Load off

3. Solar PV Energy Harvesting and MPPT

In the first mode and the third mode, the solar photovoltaic source is available. In these two modes, the maximum power point tracking is applicable. In both cases, a SMC-based MPPT is employed. The SMC helps to maintain the optimal voltage across the terminals of the SPV panel, and this is accomplished by controlling the switching actions on the buck boost converter. It is the buck mode of operation done by switch Q2 that charges the battery. Switch Q3 is used in the boost operation, and during the boost operation, the battery is discharged. Simultaneous buck and boost operations are possible. Considering switches Q2 and Q3, in the buck only mode, switch Q2 is manipulated. In the boost only mode, switches Q2 and Q3 are maintained at the same duty cycle. Switches Q2 and Q3 are operated in the buck and boost modes with different duty cycles for Q2 and Q3, and if D2 > D3 is the duty cycle for Q2 and D3 is the duty cycle

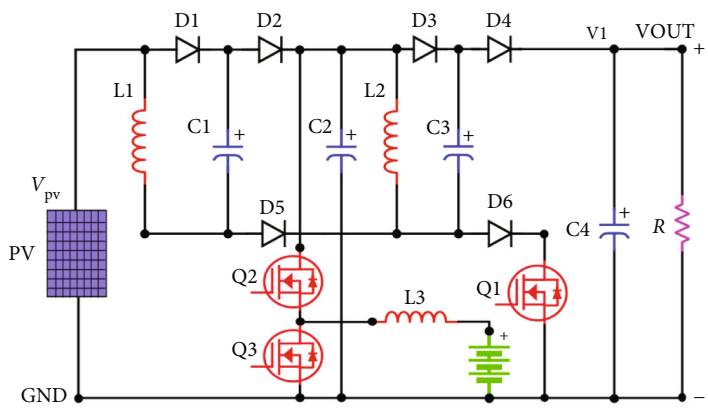

Figure 6: Topology used for Simulink realization.

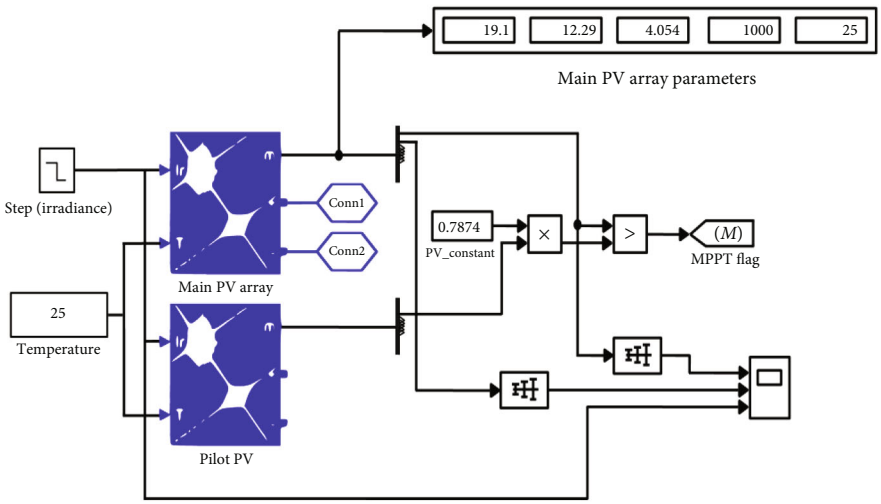

Figure 7: SPV with pilot PV modules and SMC-based MPPT.

for Q3, then the buck operation is carried out for the difference periods D2-D3 and the boost operation is carried out for the period that Q2 and Q3 are on. During the buck period, the battery is charged, and for the boost period, the battery is discharged.

The flow chart of the SMC for MPPT is shown in Figure 5. The SMC generates the flag for MPPT, and this flag in association with the switching pulses guarantees buck operation or charging operation along with the maximum power point tracking (MPPT). The proposed system accepts power from the SPV panel, charges the battery, and also delivers an output of 48 V across the load. This load is treated as the HV load. The loads that may be connected across the battery are denoted as LV loads. The regulation of the output voltage of 48 V has been carried out by a PI controller, FLC, ANN-based controller, and SMC. The performance of the control schemes has been compared and studied.

4. Simulation of the Proposed System

The primary specification of the proposed system is given in Table 1. The proposed system can be operated in three

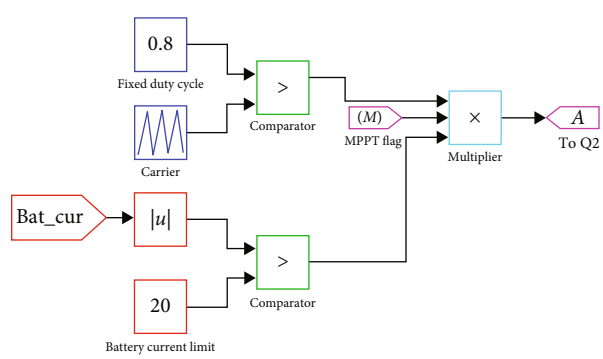

Figure 8: Control scheme for battery charging.

major modes which are considered here and shown in Table 2. In the first mode of operation, the external input DC voltage source is available sufficient enough to supply the load and charge the battery as well. In this condition, when the solar irradiance is 1000 watts per m^2, the HV channel gets 96 watts, and the battery is being charged with the remaining power of $250 - 96 = 154$ watts. In the second mode, the external input voltage source is not available

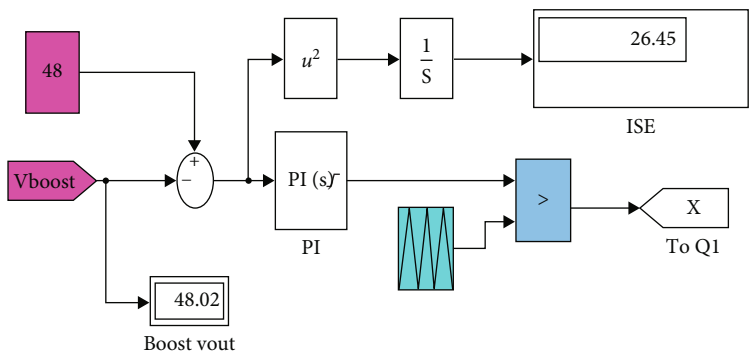

Figure 9: Switching pulse generation system by PI controller.

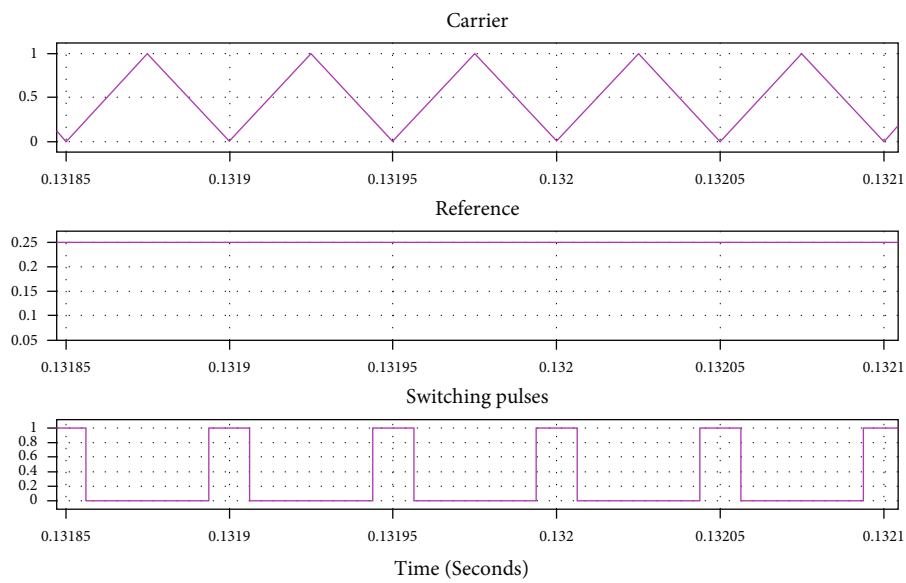

Figure 10: Carrier, reference produced by the PI controller, and switching pulses.

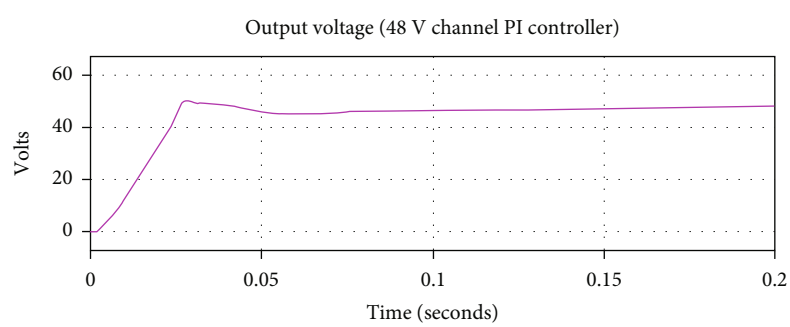

Figure 11: Output voltage regulated at 48 V.

and the battery drives the 96 watts power to the HV channel. In the third mode of operation, the external source of power is used only to charge the battery. For these three modes of operation, the transient and steady-state analysis has been carried out.

The MATLAB Simulink implementation of the proposed system is shown in Figure 6. The major subsystems are the solar PV subsystem with the SMC-based MPPT scheme, the two-stage relift Luo converter, the battery side synchronous buck boost converter, and the control subsystems. The control strategy is that the MPPT section generates a control flag that allows or blocks the buck converter that takes care of MPPT. The PI controller acting upon the switch Q1 regulates the output voltage for the load at 48 V. In place of the PI controller, the other controllers like the FLC, ANN, and P-SMC have also been studied.

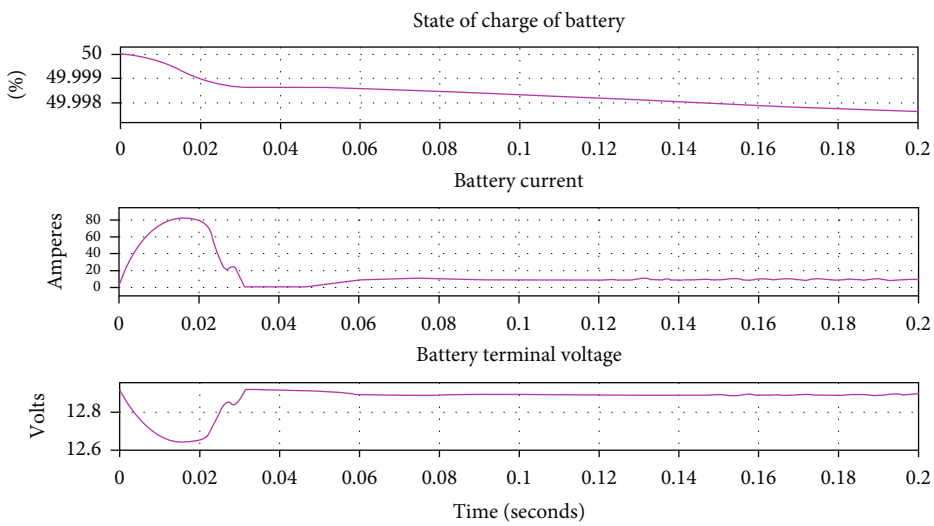

Figure 12: SOC, current, and terminal voltage of the battery for PI controller.

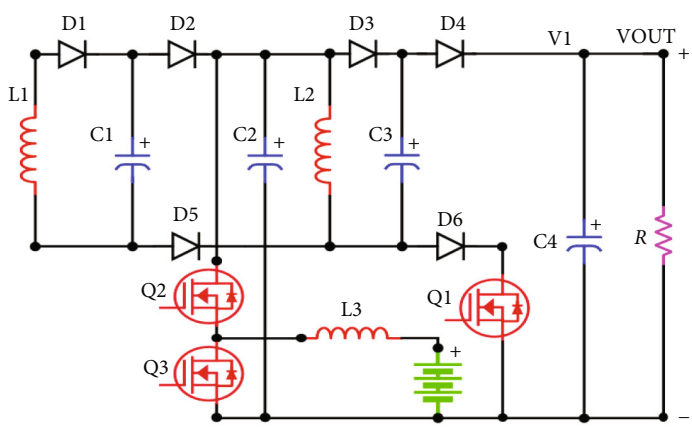

Figure 13: Topology without SPV realized in Simulink.

Figure 7 shows the SPV panel and the SMC-based MPPT subsystem which produces the control flag. The generation of switching pulses for the buck converter switch Q2 is shown in Figure 8. With reference to simulation model (Figure 8), the carrier frequency is 20 kHz and the duty cycle is kept at a constant level of 0.8. The comparator produces a train of square pulses with a duty cycle of 0.8. The switching pulses can reach the switch Q2 if and only if the MPPT flag and the current limiter flag are at logic 1 level. If any of these constraints fail and become logic 0, then the switching pulses do not reach Q2 and the buck section used for charging the battery is turned off.

4.1. Realization of PI Controller. A PI controller for the regulation of the output voltage at 48 V was developed in the Simulink environment. The block schematic of the PI controller realized in MATLAB Simulink is shown in Figure 9. The PI controller has been tuned with Kp = 0.1 and Ki = 1. This PI controller along with the switching pulse generation system is used for the power electronic switch Q1 which is responsible for delivering power to the output with the output voltage regulated at 48 V. With reference to Figure 9, the error between the set point of 48 V and the actual output voltage is obtained first. Then, the error is fed to the PI controller. The output of the PI controller is the reference used in the PWM section where a 20 kHz triangular wave is used as the carrier. The square pulses generated by the PWM comparator drive the power electronic switch Q1 used in the 48 V output channel. The error is further squared and integrated to get the integrated square error (ISE) used as a performance index.

The triangular carrier wave with 20 kHz, the reference signal produced by the PI controller, and the PWM pulses generated are shown in Figure 10. The trajectory of the output voltage and the battery-related measurements are shown in Figures 11 and 12. As shown in Figure 11, there is a small overshoot of 2.5 V with a steady-state error of 0.2 V and an accumulated ISE of 26.45.

The results shown in Figures 11 and 12 have been obtained when the solar PV source is not available and the output is completely served by the battery. The circuit's topology is when the SPV is unavailable and the load is being supplied by the battery, and Figure 13 shows the Simulink realization of the proposed system without SPV.

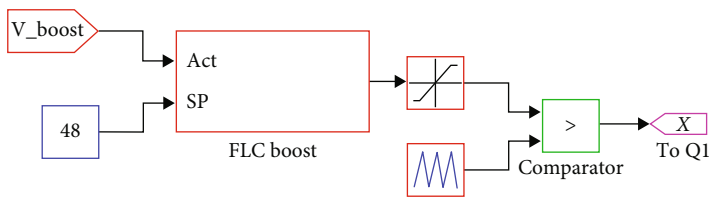

Figure 14: Switching pulse generation using FLC for switch Q1.

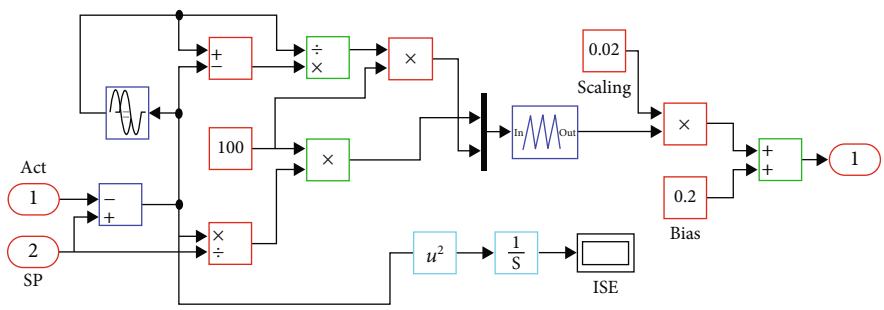

Figure 15: Structure of the FLC realized in MATLAB Simulink.

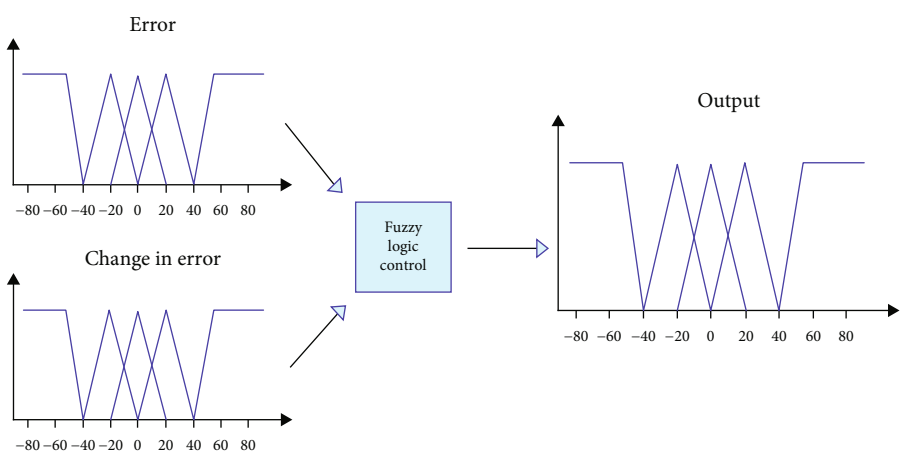

Figure 16: Membership functions of FLC.

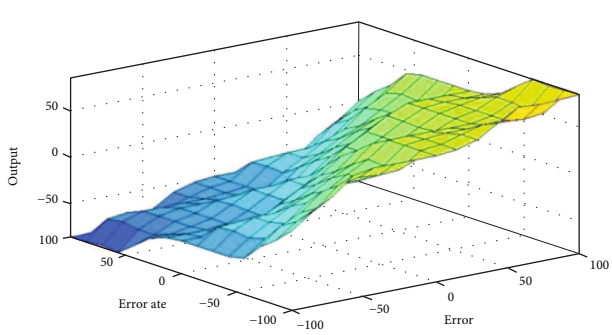

Figure 17: Surface of rule base used in the FLC.

4.2. Realization of Fuzzy Logic Controller. Fuzzy logic controller (FLC) is a control technique which helps to arrive at an acceptable result with approximate data. The FLC is capable of providing a practically acceptable and useful controller performance, and the FLC can be designed even when a precise mathematical of the system to be controlled is not available. The FLC is intelligent and is adaptive. It uses the human experience imparted to the control scheme in the form of a knowledge base or rule base. The various steps used in the development of the FLC are the scaling, segmentation, and fuzzification.

The fuzzified date is fed to the fuzzy engine. The fuzzy engine uses the data in the fuzzy form, and the decisions are supplied as output of the FLC in the fuzzy form. The defuzzification step recovers the real-time control data that is used for generating the reference signal used in the PWM section. The Simulink realization of the FLC blocks, for the regulation of the output voltage at 48 V level, is shown in Figures 14 and 15. With reference to Figure 14, the input to the FLC is the set point and the actual voltage level at the output. The output of the FLC is used as the reference in the PWM section where the reference is compared

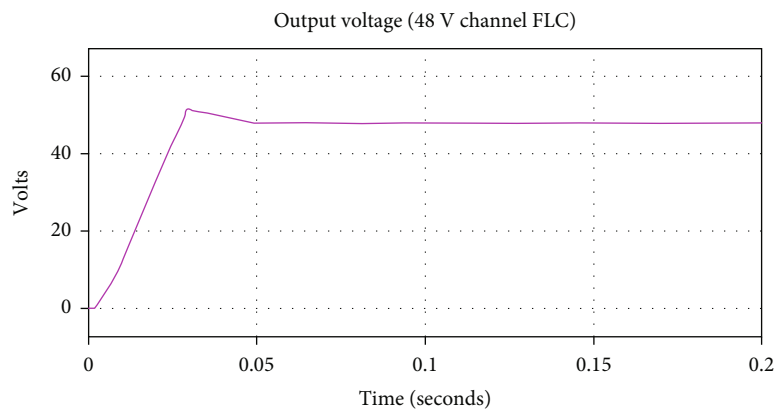

Figure 18: Output voltage with the FLC.

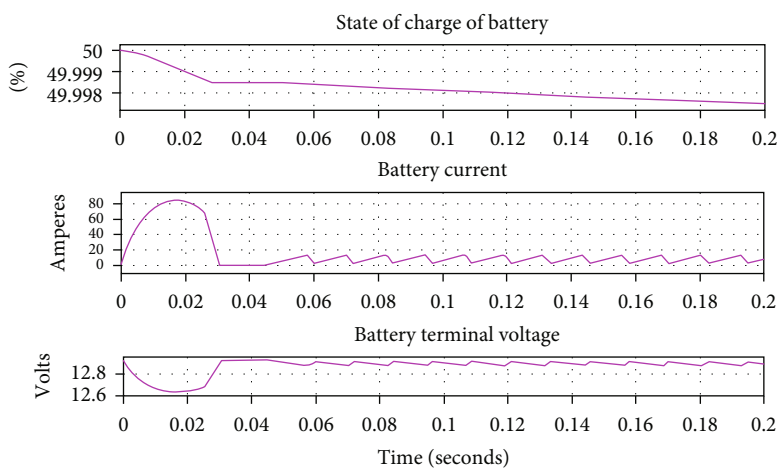

Figure 19: SOC, current, and terminal voltage of the battery with FLC.

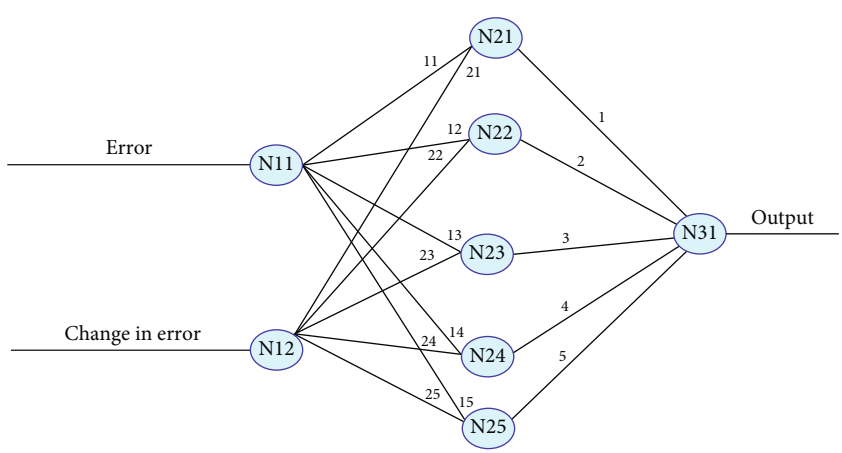

Figure 20: Structure of the multilayer feed forward ANN.

against a 20 kHz triangular carrier to produce the switching pulses for boost section switch Q1.

The results are obtained while using the FLC for the regulation of the output voltage. Usually, the error and the change in error are the two inputs supplied to the fuzzy engine, and these two inputs are fuzzified as per the membership functions shown in Figure 16. The surface of the rule base is shown in Figure 17.

The results shown in Figures 18 and 19 have been obtained when the SPV source is not available, and the output is completely served by the battery. As shown in Figure 18, there is a small overshoot of 1.5 V with a steady-

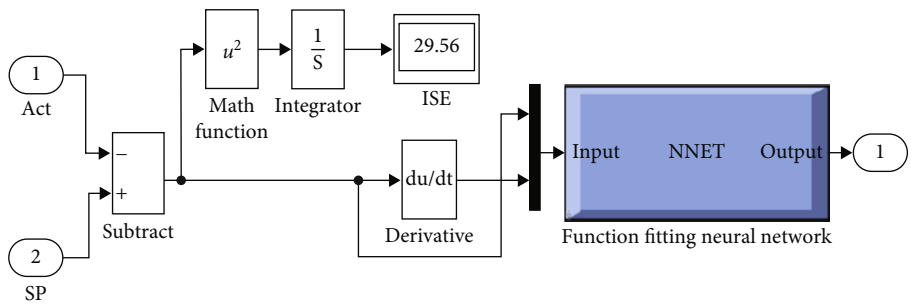

Figure 21: Position of the ANN unit in the ANN-based controller.

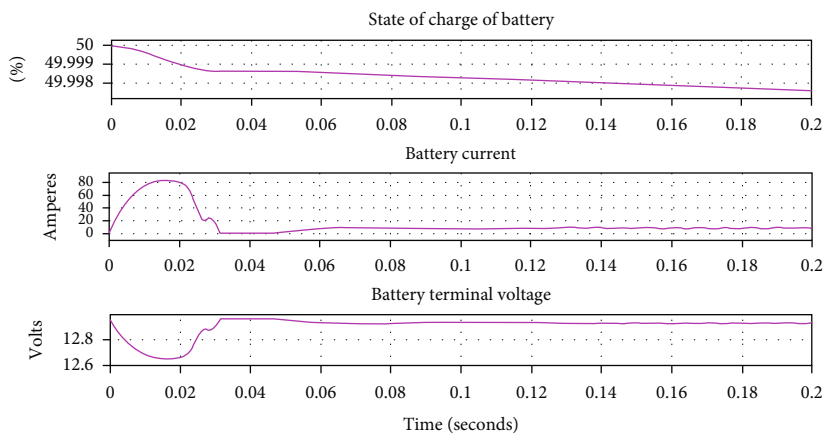

Figure 22: SOC, current, and terminal voltage of the battery with ANN.

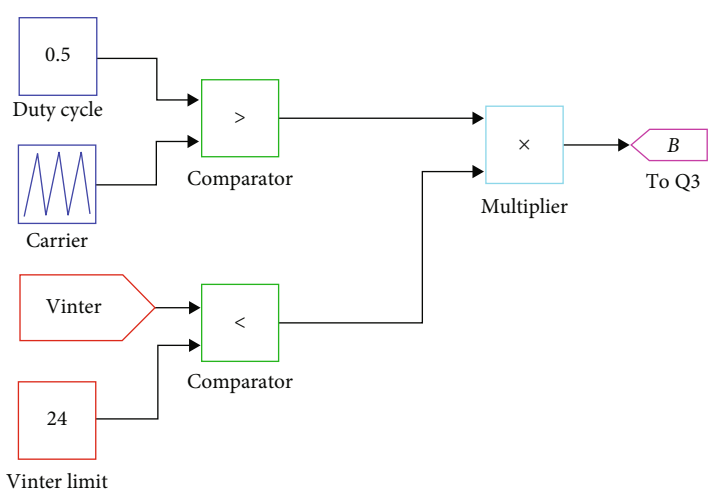

Figure 23: Control scheme for regulating the intermediate voltage.

state error of 0.2 V and an accumulated ISE was observed to be 26.05.

4.3. Realization of ANN-Based Controller. The ANN (artificial neural network) can be used for control applications where it can be trained to act as already tuned controllers while improving the dynamic performance by virtue of making fast decisions. For example, the FLC makes control decisions based on the error and change in error in association with a rule base. Making decisions based on the rule base takes a fairly long time, and this may deter the dynamic performance in fast systems like power electronic converters. The ANN can be a replacement for the FLC with the functionality of the FLC imparted to the ANN by way of training. An ANN trained to function as an FLC offers the advantages of making the best decisions like the FLC but comparatively faster than the FLC itself. This principle is used in this work, and an ANN-based controller has been built, and its performance studied and compared with other control schemes was discussed in this work.

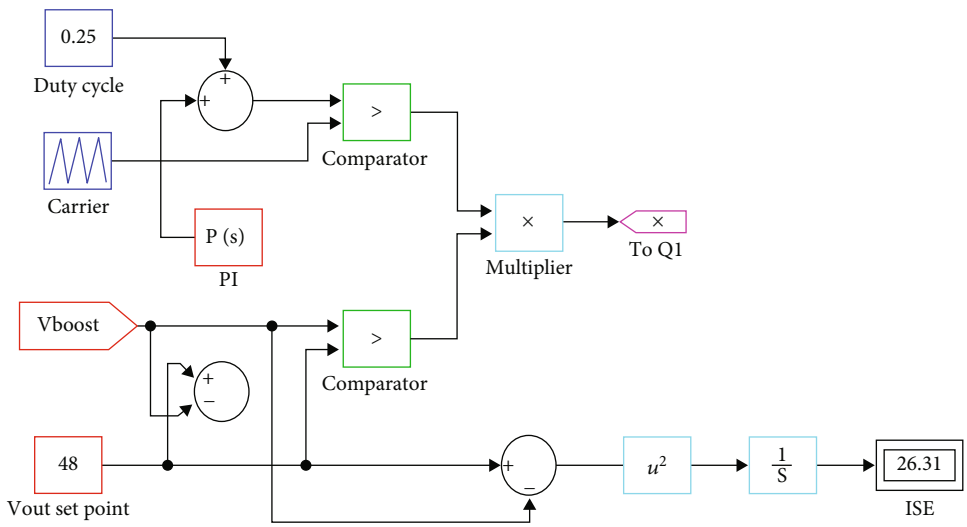

Figure 24: Modified sliding mode controller.

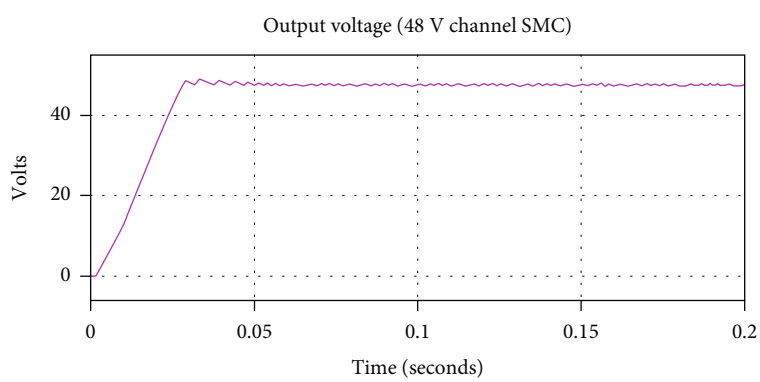

Figure 25: Output voltage with P-SMC controller.

The ANN is a network of neurons arranged in the form of layers as shown in Figure 20. Each layer has a definite number of neurons. All the neurons in the first layer are connected individually to all the neurons in the second layer and so on. In this work, a three-layer network is used. The first layer is the input layer, the second layer is the hidden layer, and the third layer is the output layer. The error and rate of change of error are the two inputs, and the input layer has two neurons. The hidden layer uses 20 neurons, and the output layer has a single neuron, and it gives the duty cycle. The implementation of the ANN-based controller is shown in Figure 21. Some of the important results obtained for regulating the output voltage at 48 V while drawing power from the battery are shown in Figure 22.

4.4. Realization of Proportional SMC Controller. Power electronic converters are nonlinear systems since they use nonlinear elements like diodes and switches. Depending upon the on or off states of the switches, several topological formations are obtained, and each of them is linear. Thus, the converter can be treated as a variable structure system, and the different structures are produced by the states of the switches. The SMC is the naturally suitable candidate controller for the variable structure systems. In this work, SMC used two different applications. The first one is that an SMC is used for the MPPT control of the SPV panel. The second application of SMC in this work is for the regulation of the output voltage at 48 V. The control law adopted by the SMC is simple, and the steps involved are shown herein:

(1) Accept the set point voltage for output (SP)

(2) Measure the actual output voltage (Act)

(3) If Act < SP, turn on the control flag

(4) If Act > SP, turn off the control flag

With the SMC, the switching pulses are generated with a fixed duty cycle. The duty cycle is so selected such that the output voltage can be raised from zero output voltage to the vicinity of the set point. The phase that ranges between the zero output voltage and until it reaches the set point is called the reaching phase. The duty cycle selected should be able to complete the reaching phase and bring the output voltage equal or more than the set point voltage. The SMC control flag is logic 1 during the reaching phase. Once the

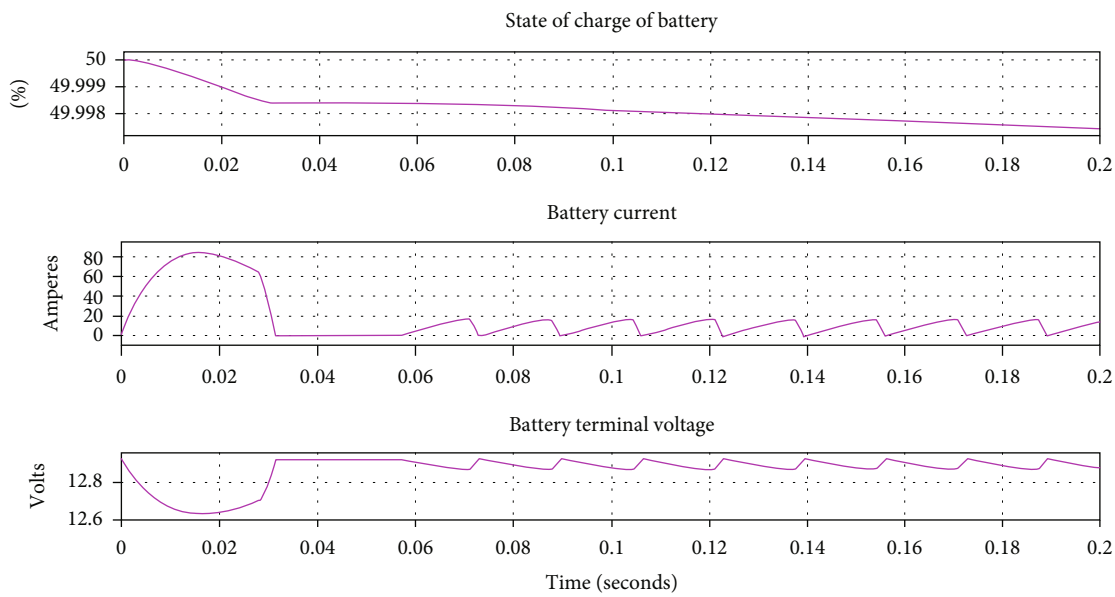

Figure 26: SOC, current, and terminal voltage of the battery with P-SMC.

actual output voltage crosses the set point voltage, the SMC control flag is reset to logic 0. This stops the supply of switching pulses from reaching the gate of the power electronic switch. As soon as the output voltage reaches slightly below the set point, the SMC control flag changes back to logic 1, and switching pulses are once again applied to the power electronic switch. This action continues, and the output voltage just moves up and down the set point voltage with a very small margin above and below the set point. The area formed along the time axis with the extremities of the trajectory above and below the average value is called the sliding surface.

In the proposed scheme, when the system is operating without the SPV source available, the battery is the only source to deliver the 96 watts power to the load. The synchronous buck boost converter's boost arrangement in the battery portion is active switch Q3 delivering a 24 V intermediate DC voltage across capacitor C2. This helps to reduce the duty cycle of the second stage of the relift converter. The realization of the SMC in MATLAB Simulink for the regulation of V_{inter} maintained across C2 is shown in Figure 23. The second sliding mode controller used for switch Q1 has a modification. Instead of maintaining a fixed duty cycle as done for the intermediate stage, the final stage SMC uses a P controller that also determines the marginal variations required for the duty cycle from a centre value of 0.25. The modified or hybrid P-SMC is shown in Figure 24. Some of the important waveforms associated with the SMC for the output voltage regulation are shown in Figures 25 and 26.

4.5. Battery Charging Mode. With battery, there are two modes possible. In one of the two modes of operation, the 96 watts/48 V load is disconnected. The SPV source is used exclusively for charging the battery. The control scheme adopted for this condition is shown in Figure 27. The buck

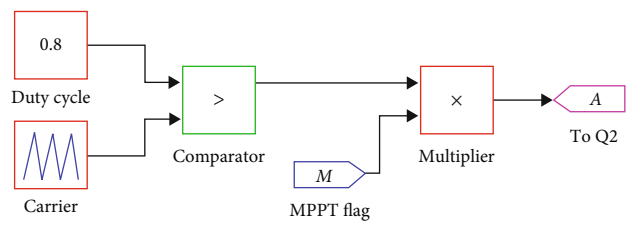

Figure 27: Switching pulse generation for switch Q2.

converter switch Q2 in the synchronous buck boost converter acts as the power controller, and the switch Q3 is turned off and is used as the freewheeling diode. The SMC for MPPT with the flow chart is shown in Section 3. It is implemented, and the MPPT flag is generated. This flag is used in the control unit for the battery charging buck converter switch Q2 as shown in Figure 27. The case of a step change in solar irradiance of 1000 watts per m^2 to 500 watts per m^2 occurring at time instant 0.2 seconds is considered, and the related waveforms are shown in Figure 28.

Further, in the second mode, the case of the ample solar power being available while the output voltage of 48 V is being regulated and simultaneously the battery is also charged has been studied. Figure 29 shows the switching pulses for Q2 and Q3 belonging to the synchronous buck boost converter and for the switch Q1 used in the relift Luo converter. With reference to Figure 30, the SOC of the battery rises at a faster rate until the time instant 0.2 seconds because until time instant 0.2 seconds, the solar irradiance is 1000 watts per m^2. Until 0.2 seconds, the charging current is higher reaching a maximum of 8 A. After 0.2 seconds, the charging current falls and gets reduced to about 0.8 A. In a similar manner, the terminal voltage of the battery is also higher until time 0.2 seconds and falls marginally after 0.2 seconds.

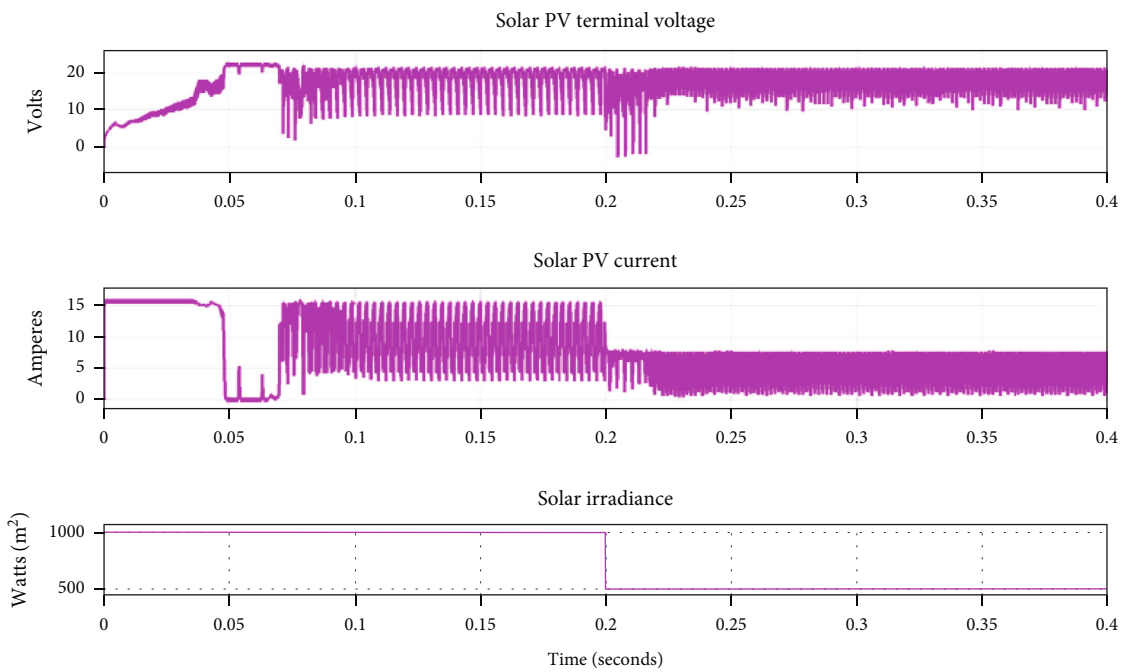

Figure 28: SPV voltage and current with respect to step change in solar irradiance.

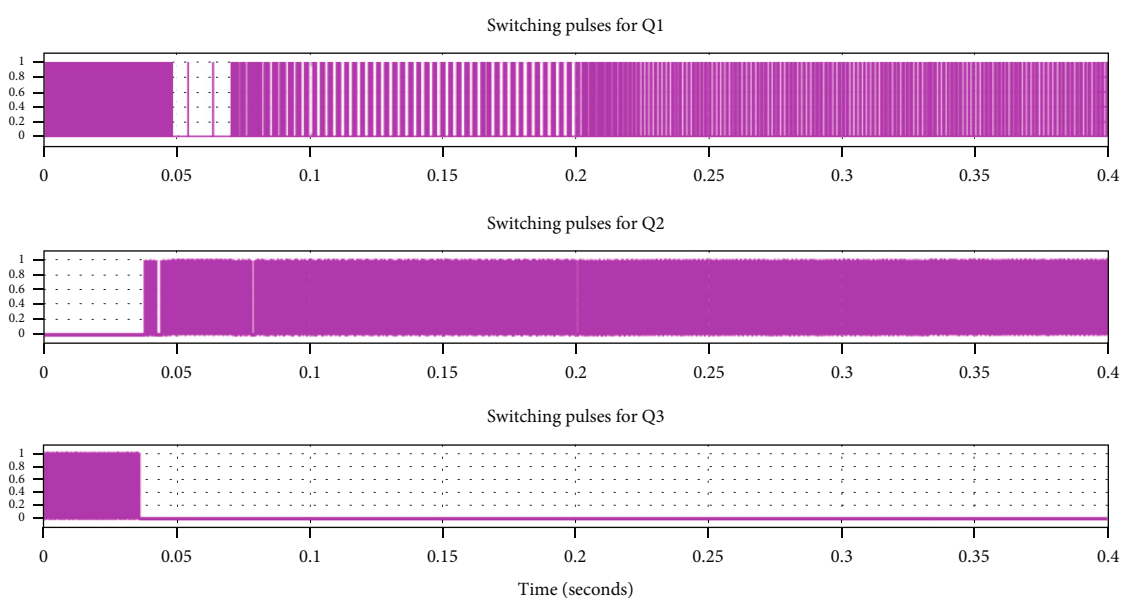

Figure 29: Switching pulses for Q1, Q2, and Q3.

The trajectory of the output voltage across the 48 V channel is shown in Figure 31. It can be noted from Figure 31 that during the period for which the solar irradiance is 1000 watts per m^2, the output voltage exhibits more ripple. Beyond time instant 0.2 seconds, the solar irradiance falls to 500 watts per m^2 and the charging action gets reduced and the output voltage is smoother with reduced ripple. This phenomenon is clearly seen in Figure 31.

A study of the battery charging action alone while the 48 V channel was stopped has also been carried out. Figures 32–34 show the waveforms of various parameters during the battery charging action when the 48 V channel is not active and there is no other load. The buck converter switch Q1 is active. It is controlled by the sliding mode controller MPPT with a maximum duty cycle set at 0.8. With reference to Figure 32, the rate of rise of SOC of the battery is higher as long as the solar irradiance is 1000 watts per m^2; after the solar irradiance falls to 500 watts per m^2, the rate of rise of SOC of the battery gets reduced. The charging current reaches a maximum of 15 A before 0.2 seconds and gets

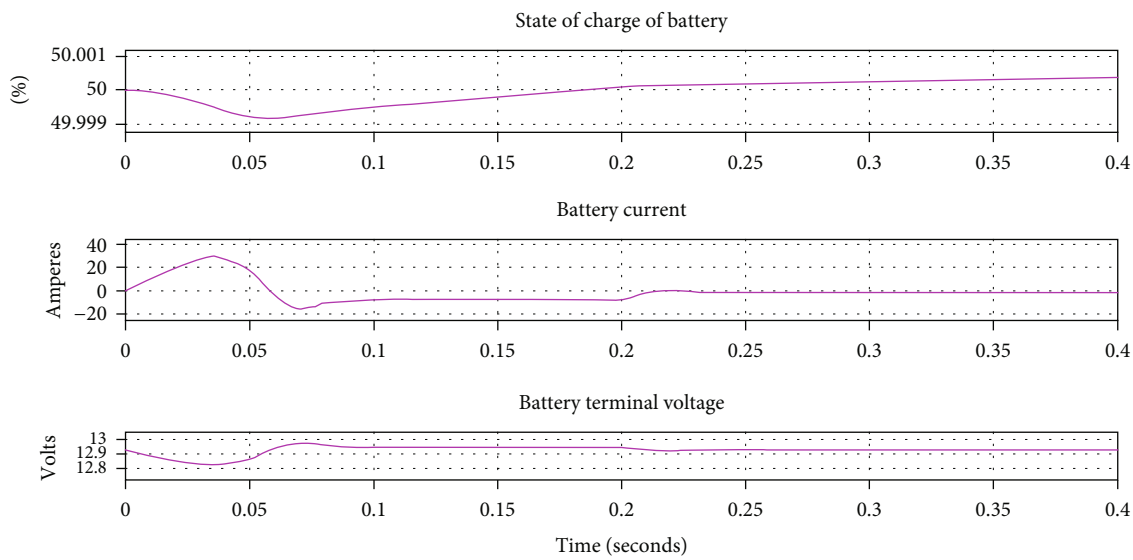

Figure 30: SOC, current, and terminal voltage of the battery for time instant of 0.2 seconds.

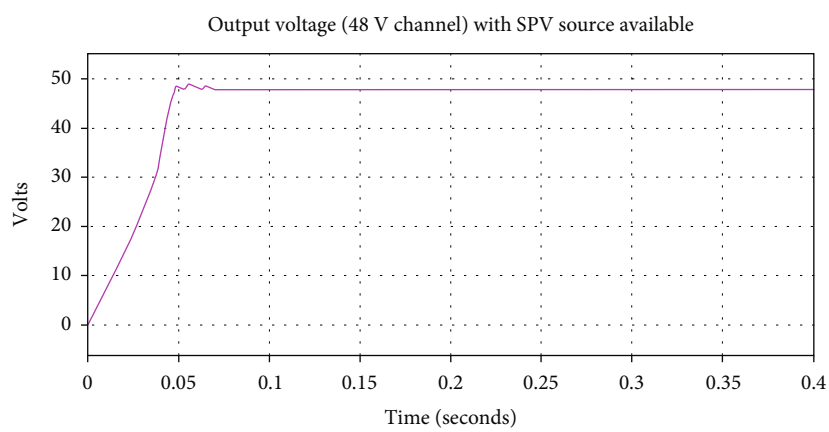

Figure 31: Regulated output voltage while SPV is available and the battery is charged.

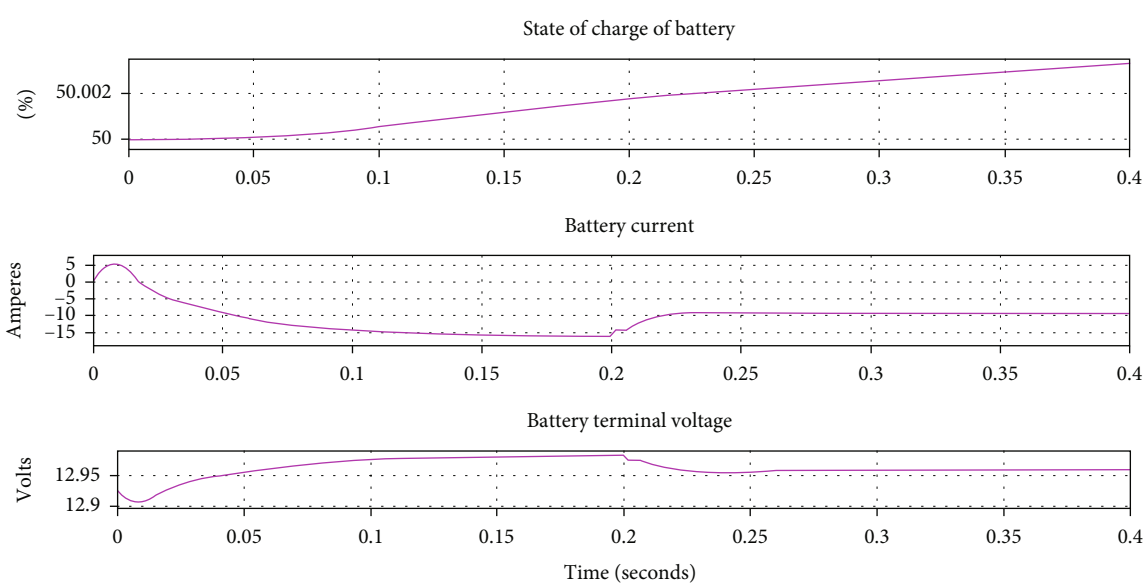

Figure 32: SOC, current, and terminal voltage of the battery (only battery charging).

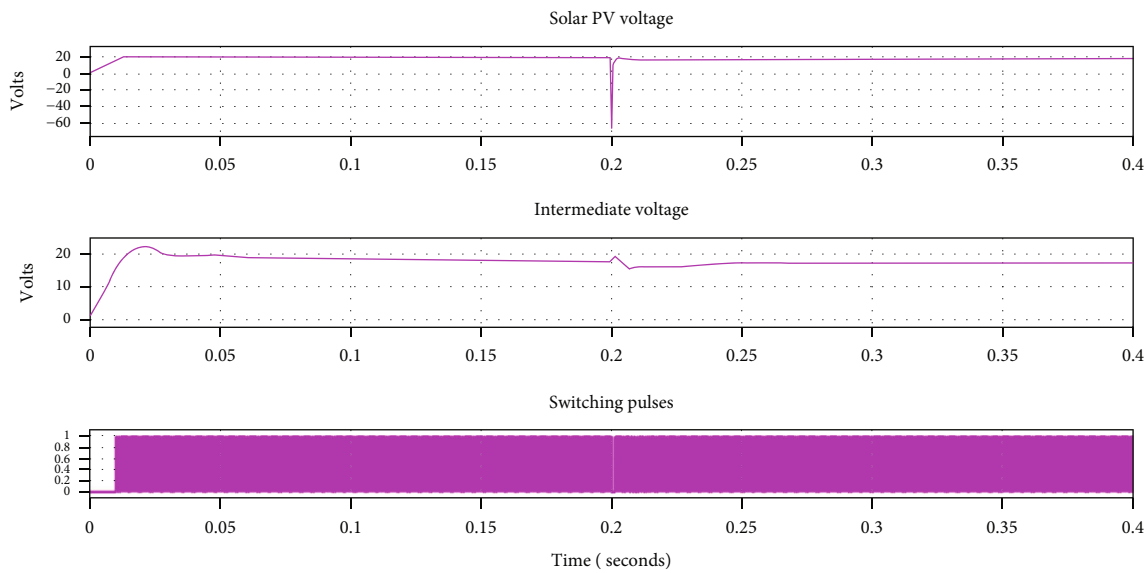

Figure 33: SPV terminal voltage, voltage across C2, and switching pulses for Q2.

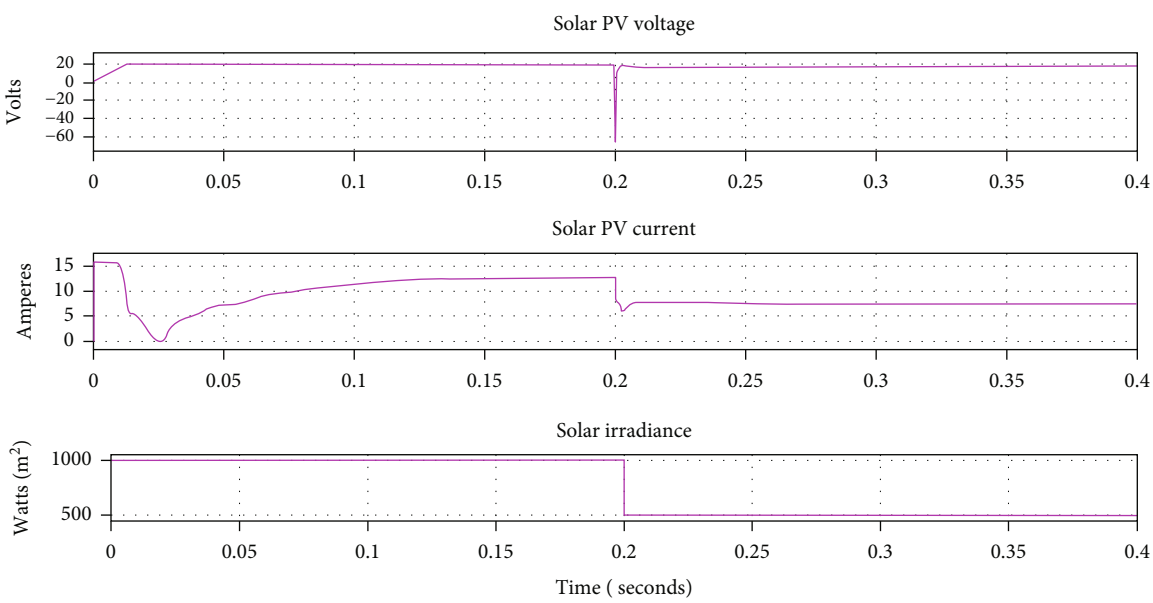

Figure 34: Solar irradiance and the corresponding SPV voltage and SPV current.

Table 3: Comparison of performance indices.

Control strategies	Rise time (sec)	Steady-state error (volts)	Overshoot (volts)	ISE	Ripple (volts)
PI controller	0.03	0.02	9%	26.45	0.2
FLC	0.03	0.02	1.5%	24.2	0.2
ANN	0.03	0.035	1.2%	25.7	0.35
P-SMC	0.03	0.02	1.2%	26.31	0.2

reduced after the 0.2 seconds instant and reaches nearly 8 A. Accordingly, the terminal voltage of the battery is also altered as shown in Figure 32.

The trajectory of the voltage across the SPV panel; the intermediate voltage, after the first lift stage, that appears across capacitor C2; and the switching pulses applied to Q2 is shown in Figure 33. During the initial start-up period, the SPV source is used for charging the capacitors and this causes a heavy SPV current and its voltage is much less than the reference voltage applicable for MPPT at the given solar

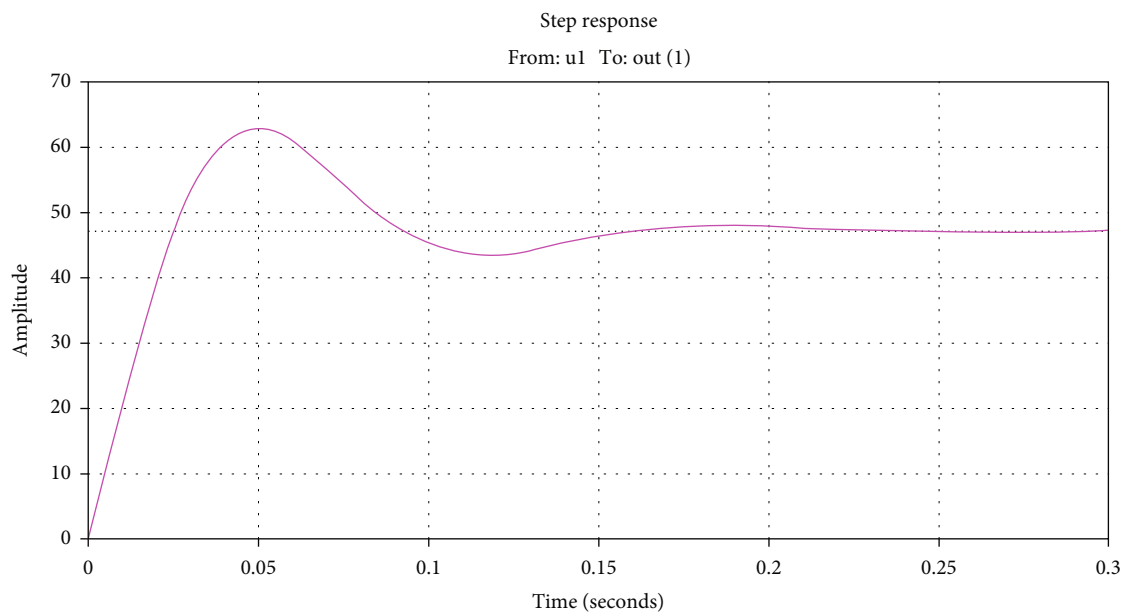

Figure 35: The step response of the system denoted as sys.

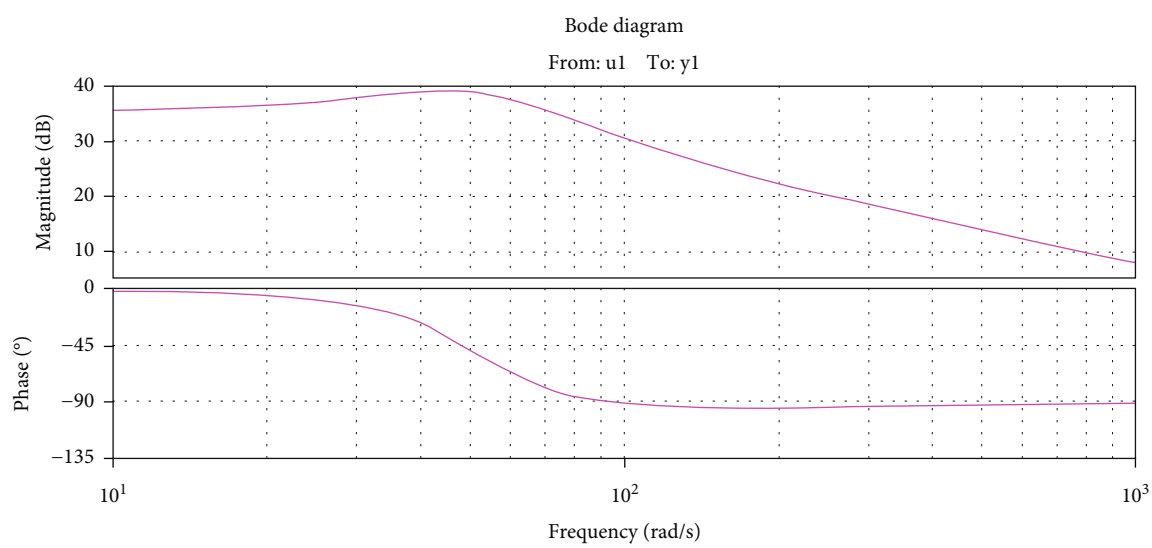

Figure 36: The Bode plot of sys.

irradiance of 1000 W per m^2. This causes the MPPT flag to be at logic low level, and the switching pulses are not allowed to the buck switch Q2. This aspect is shown in the waveform of the switching pulses in Figure 33.

The solar irradiance, SPV voltage, and SPV current are shown in Figure 34. With reference to Figure 34, the power output of the PV panel during the period for which the solar irradiance is 1000 watts per m^2 is 20*12.8 = 256 W. During this time, the battery receives electricity, and the terminal voltage of the battery multiplied by the charging current is 12.98*16 = 208 W. This accounts a power conversion efficiency of 81.25%. Similarly, with reference to Figure 34, the power output of the PV panel during the period for which the solar irradiance is 500 W per m^2 is 19.9*7.5 = 149.25 W. The power delivered to the battery, during this period, is 12.96*10 = 129.6 W, and the corresponding power conversion efficiency is 86.83%. The performance indices obtained in the regulation of the output voltage at 48 V with different control schemes have been recorded and tabulated as shown in Table 3.

4.6. Stability Analysis of the Proposed System. The closed loop output voltage regulation under normal circumstances has been well demonstrated by many researchers already. Therefore, the stability of the output voltage regulation while fed from the battery is considered for a critical study. This mode of operation involves the second stage of the Luo converter and the boost stage of the buck boost battery control subsystem. In order to make a through cybernetic stability analysis of this mode of operation, the system transfer

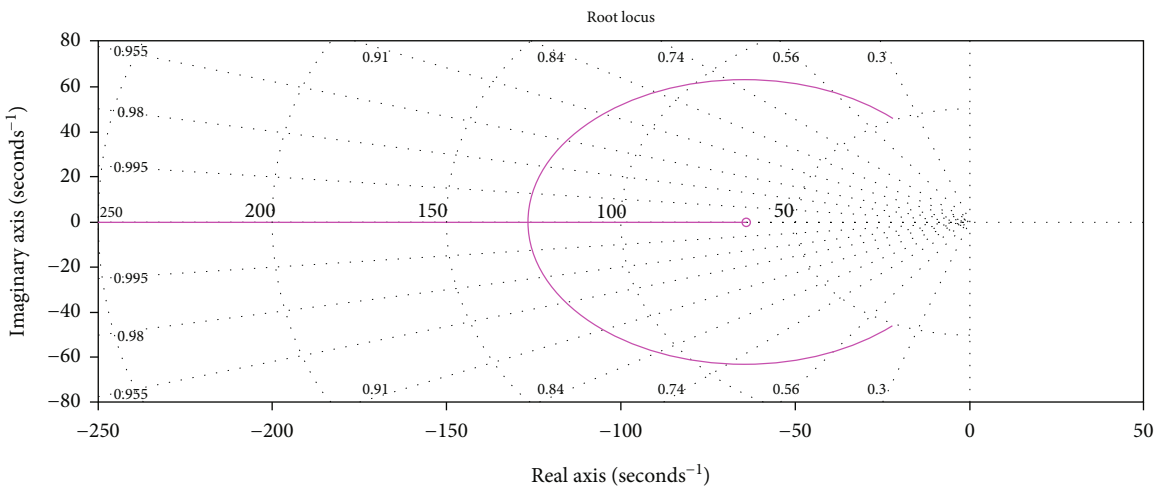

Figure 37: The root locus of sys.

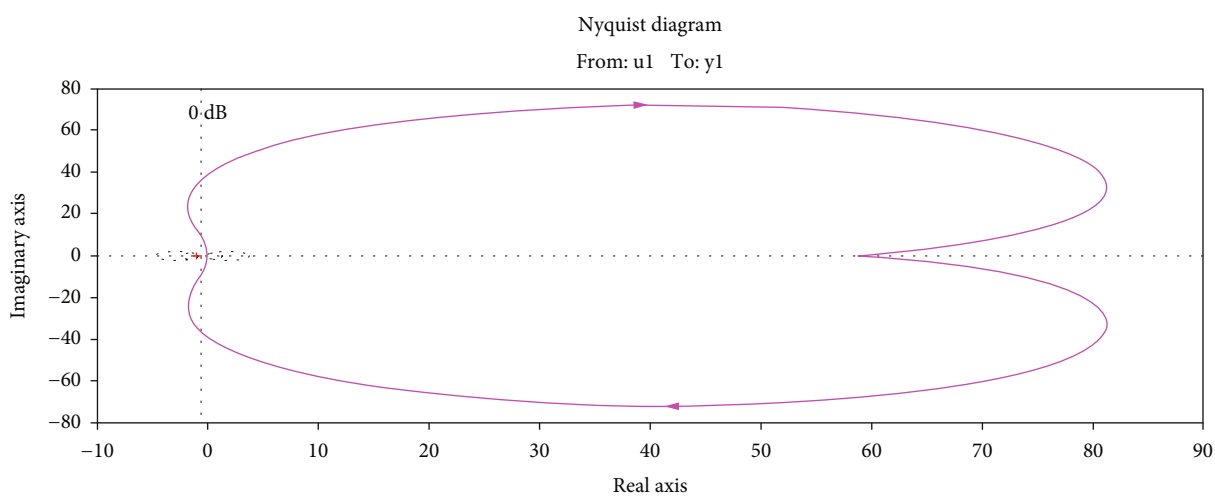

Figure 38: The Nyquist plot of sys.

function has been obtained. The transfer function has been obtained between the output voltage and the duty cycle used in the controller as applied to the boost MOSFET of the battery subsystem. The variables "vout" and "duty" were used for the output and the input, respectively. The following commands were invoked from the command line of MATLAB:

```
>>mysys = idadta(vout,duty,0.0001)
>>sys = tfest (iddata,2)
```

The following transfer function was obtained:

$$\text{sys} = \frac{2444\,S + 1.56e5}{S^2 + 43.71s + 2651}. \tag{7}$$

After getting the transfer function as sys, the following commands were invoked and the results obtained are shown. The step response of the system for a duty cycle of 0.8 has been obtained as shown in Figure 35. The Bode plot, the root locus, and the Nyquist plot all indicate that the closed loop system is completely stable.

Figure 39: Photograph of the prototype.

Figures 36–38 show the Bode plot, root locus, and Nyquist plot of sys. The Bode plot reveals sufficient gain and phase margins. The root locus reveals that the two poles lie on the left half of the complex plane. The Nyquist plot does not circle the -1 point along the x axis, and these observations have clearly established that the system is asymptotically sable.

Table 4: Specifications of the SPV.

Parameters	Value
Solar PV source	
Nominal power rating	125 watts
Open circuit voltage per panel	22.07 V
Short circuit current	7.86 A
Voltage at Pmax	17.38 V
Current at Pmax	7.43 A
Volt @ Pmax/volt VOC	17.38/22.07 = 0.7875
Test condition	1000 W/m^2, 25°C

Table 5: Specifications of the SLLC, battery, and HV load.

Parameters	Value
Relift Luo converter	
Inductors L1–L4	1 millihenry
Capacitors C1–C5	470 microfarad
Switches Q1–Q3	IRF540
Diodes D1–D8	FR607
Battery	12 V, 35 Ah (lead acid)
HV 48 V load	48 - 24 E 48 W - 96 W
Switching frequency	5 kHz

5. Experimental Verification

The proposed idea has been validated with an experimental prototype. Figure 39 shows the photograph of the experimental setup. A solar panel of rating 125 W was used as the source of power for the experimental setup. The nominal terminal voltage of the SPV panel was 17.5 V. The main output voltage was required to be regulated at 48 V across a 24-ohm resistor. A lead acid battery of 35 Ah with a nominal terminal voltage of 12 V was used. The IRF540 MOSFET were used as the power electronic switches, and the optocoupler IC MCT2E were used for providing the required isolation between the source side and the load side. Table 4 shows the specifications of the SPV, and Table 5 shows the specifications of the SLLC, battery, and HV load system.

With the available SPV source, when the solar irradiance was nearly 960 W/m^2, the battery was charged, and also, the output voltage across the 24-ohm load was maintained at 48 V. The pattern of the switching pulses applied to the relift Luo converter is shown in Figure 40, and the terminal voltage across the SPV module was 19.9 V and is shown in Figure 41. In order to make the source current, an additional filter of 10 microhenries was introduced in series with the source and the source current was observed to be continuous as shown in Figure 42.

The output voltage is regulated at 48 V, and the waveform of the output voltage is shown in Figure 43. A variation of load from 24 ohms to 48 ohms has been introduced at time instant 6.2 seconds, and the slight disturbance in the output voltage was observed. This transient behavior of the sudden change in load is visible in Figure 43.

Figure 40: Switching pulses for buck switch.

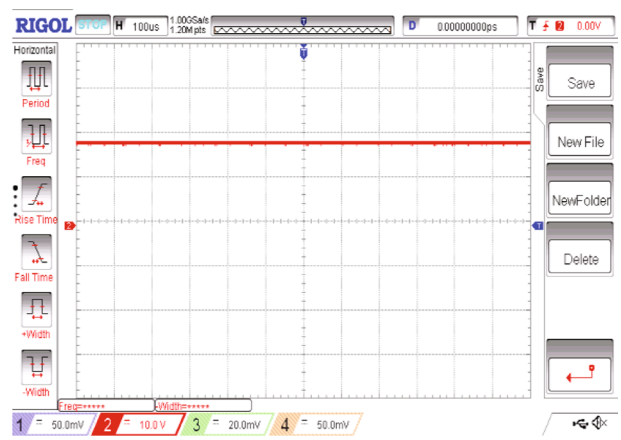

Figure 41: SPV terminal voltage.

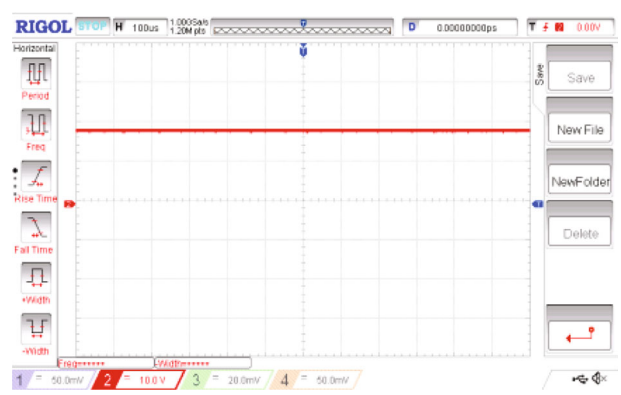

Figure 42: Source current.

5.1. Performance Analysis of the Proposed Converter. Although the system uses 3 switches and six diodes, they are distributed into different subsystems. Actually, the superlift Luo converter uses only one switch. And this is usual. The battery charging buck boost converter uses two switches, and this is also usual. There are several modes of operation, and not all the three switches are operational in all modes of operation.

For example, the superlift converter is operational while the solar PV source is sufficiently available to drive the load. During this mode of operation, if the battery is also full, then

Figure 43: Output voltage regulated at 48 V channel.

neither charge or discharge action takes place. Only the switch associated with the superlift Luo converter is operational. In this mode of operation, the efficiency with simulation was observed to be 89% with simulation and 84% with experimental prototype.

In another mode of operation, the final load may not be required to be operated and only the battery is being charged. In this case, only the buck converter switch in the buck boost converter is operational and the boost switch is in the off state. The efficiency of battery charging was observed to be 87% in simulations and 82% in experimental verifications.

Only in one mode of operation, the boost switch of the buck boost converter and the superlift Luo converter switch are operational. This occurs when there is no solar power available and the battery is being used to drive the load. Only during this condition, since two switches are operational, the efficiency of power conversion between the battery and the load is little reduced, but even in this case, it was observed in simulations as 82% and 80% in experimental prototype.

Further, as for the diodes, the superlift Luo converter uses 6 diodes. But in this application, the converter is split into two sections, and midway, the buck boost converter is connected for battery charging and discharging. Therefore, in the three modes of operations considered, only when the solar power feeds the load, the six diodes are operational. In the battery charging mode while the load is not operational, only the first part of the lift converter is used. Similarly, when the solar PV source is not available, it is the battery that drives the load through the second part of the lift converter. Thus, only in one mode, six diodes are operational, and in the other two modes, only three respective diodes are used. Thus, the power conversion efficiencies of the system in different operational modes are different and are good.

6. Conclusion

The proposed dual-output DC to DC converter built around a relift Luo converter has been developed as a circuit model in the MATLAB Simulink environment. The proposed system was tested in three different modes. In the first mode, the solar irradiance was set at 1000 W/m^2. Out of the harvested power of 250 W, 96 W was delivered to the 48 V load and the remaining power was used for charging the battery. In the second mode, the solar power was not used. The battery was used to drive the 96 W load with a closed loop output voltage regulatory system to regulate the output voltage at 48 V. The performance of a PI controller, an FLC, an ANN-based controller, and a proportional SMC was studied and compared. The peak overshoot, the settling time, the steady-state error, and the integral square error were compared. The SMC-based output voltage regulatory system has been found to outperform other control schemes. In the third mode of operation, the solar PV source was used to charge the battery completely. The complete power harvested from the solar PV source had been used for charging the battery with sliding mode controlled maximum power point tracking. All the proposed ideas have been verified using circuit simulations in MATLAB, and the sliding mode controlled closed loop control scheme for the regulation of the output voltage had been verified using experimental prototype also. As compared to the existing boost-derived dual-output converter, the proposed scheme is proved to be more advantageous with increased voltage gain. It has been shown that the usage of the sliding mode controller for MPPT as well as for regulating the output voltage has been more effective. It has been established that the relift converter can be used for deriving an additional output voltage channel in between the cascaded stages of the relift topology with no extra switches.

Data Availability

No data were used in this article.

Conflicts of Interest

The authors declare that they have no conflicts of interest.

Authors' Contributions

R. Banupriya wrote and edited the manuscript and was responsible for the design, MATLAB and hardware implementation, performance analysis, and result discussion. R. Nagarajan wrote and edited the manuscript and was responsible for the design, MATLAB and hardware implementation, performance analysis, and result discussion. K.R.N. Kalis was responsible for the MATLAB and hardware implementation, performance analysis, and result discussion. All authors contributed to the simulation and experimental validation of the research work.

References

[1] Y. M. Chen, A. Q. Huang, and X. Yu, "A high step-up three-port DC-DC converter for stand-alone PV/battery power systems," *IEEE Transactions on Power Electronics*, vol. 28, no. 11, pp. 5049–5062, 2013.

[2] B. R. Lin and C. W. Chu, "Hybrid DC–DC converter with high efficiency, wide ZVS range, and less output inductance," *International Journal of Circuit Theory and Applications*, vol. 44, no. 5, pp. 996–1011, 2016.

[3] N. A. Dung, P. P. Hieu, Y. C. Hsieh, J. Y. Lin, Y. C. Liu, and H. J. Chiu, "A novel low-loss control strategy for bidirectional DC–DC converter," *International Journal of Circuit Theory and Applications*, vol. 45, no. 11, pp. 1801–1813, 2017.

[4] A. Choudhury, P. Pillay, and S. S. Williamson, "Comparative analysis between two-level and three-level DC/AC electric vehicle traction inverters using a novel DC-link voltage balancing algorithm," *IEEE Journal of Emerging and Selected Topics in Power Electronics*, vol. 2, no. 3, pp. 529–540, 2014.

[5] J. Malan and M. J. Kamper, "Performance of a hybrid electric vehicle using reluctance synchronous machine technology," *IEEE Transactions on Industry Applications*, vol. 37, no. 5, pp. 1319–1324, 2001.

[6] R. Faraji and H. Farzanehfard, "Soft-switched nonisolated high step-up three-port DC-DC converter for hybrid energy systems," *IEEE Transactions on Power Electronics*, vol. 33, no. 12, pp. 10101–10111, 2018.

[7] S. S. Dobakhshari, J. Milimonfared, M. Taheri, and H. Moradisizk, "A quasi-resonant current-fed converter with minimum switching losses," *IEEE Transactions on Power Electronics*, vol. 32, no. 1, pp. 353–362, 2017.

[8] E. Babaei, Z. Saadatizadeh, and P. C. Heris, "A new topology for nonisolated multiport zero voltage switching dc-dc converter," *International Journal of Circuit Theory and Applications*, vol. 46, no. 6, pp. 1204–1227, 2018.

[9] Z. Saadatizadeh, P. C. Heris, E. Babaei, and F. Sadikoglu, "Expandable interleaved high voltage gain boost DC-DC converter with low switching stress," *International Journal of Circuit Theory and Applications*, vol. 47, no. 5, pp. 782–804, 2019.

[10] M. Mahmoudi, A. Ajami, and E. Babaei, "A non-isolated high step-up DC-DC converter with integrated 3 winding coupled inductor and reduced switch voltage stress," *International Journal of Circuit Theory and Applications*, vol. 46, no. 10, pp. 1879–1898, 2018.

[11] K. B. Park, G. W. Moon, and M. J. Youn, "Nonisolated high step-up boost converter integrated with SEPIC converter," *IEEE Transactions on Power Electronics*, vol. 25, no. 9, pp. 2266–2275, 2010.

[12] N. Kanagaraj, M. Ramasamy, H. Rezk, and T. Manesh, "Modified bi-directional DC-DC boost converter fed three-phase four-wire PV-DVR," *Journal of Testing and Evaluation*, vol. 48, no. 4, pp. 1–29, 2018.

[13] Y. P. Siwakoti, A. Mostaan, A. Abdelhakim et al., "High-voltage gain quasi-SEPIC DC–DC converter," *IEEE Journal of Emerging and Selected Topics in Power Electronics*, vol. 7, no. 2, pp. 1243–1257, 2019.

[14] K. Sushita, N. Shanmugasundaram, K. Suriyan, R. Nagarajan, and K. Venusamy, "Impacts of residential energy storage system modeling on power system," *Sustainable Environment*, vol. 8, no. 1, 2022.

[15] N. Vázquez, C. M. Sanchez, C. Hernández, E. Vázquez, L. del Carmen García, and J. Arau, "A different three-port DC/DC converter for standalone PV system," *International Journal of Photoenergy*, vol. 2014, Article ID 692934, 13 pages, 2014.

[16] Y. Hu, W. Xiao, W. Cao, B. Ji, and D. J. Morrow, "Three-port DC-DC converter for stand-alone photovoltaic systems," *IEEE Transactions on Power Electronics*, vol. 30, no. 6, pp. 3068–3076, 2015.

[17] N. R. Nair and P. Kanakasabapathy, "A three phase grid connected SPV system using synchronverter," in *2018 8th IEEE India International Conference on Power Electronics (IICPE)*, pp. 1–6, Jaipur, India, 2018.

[18] G. K. Taneja, "GMCC based adaptive filter for SPV-RES to improve power quality in distribution grid," in *2021 4th Biennial International Conference on Nascent Technologies in Engineering (ICNTE)*, pp. 1–6, NaviMumbai, India, 2021.

[19] Y. Singh, I. Hussain, B. Singh, and S. Mishra, "Grid integration of single-phase single-stage SPV system using an active noise isolation based control algorithm," in *2016 IEEE International Conference on Power Electronics, Drives and Energy Systems (PEDES)*, pp. 1–5, Trivandrum, India, 2016.

[20] V. S. Mahadik, "Performance enhancement of SPV based water pumping with multifunction converter," in *2018 International Conference on Power Energy, Environment and Intelligent Control (PEEIC)*, pp. 392–397, Greater Noida, India, 2018.

[21] V. F. Pires, A. Cordeiro, D. Foito, and J. F. Silva, "High step-up DC–DC converter for fuel cell vehicles based on merged quadratic boost–Ćuk," *IEEE Transactions on Vehicular Technology*, vol. 68, no. 8, pp. 7521–7530, 2019.

[22] O. Ray, A. P. Josyula, S. Mishra, and A. Joshi, "Integrated dual-output converter," *IEEE Transactions on Industrial Electronics*, vol. 62, no. 1, pp. 371–382, 2015.

[23] S.-W. Lee and H.-L. Do, "Quadratic boost DC–DC converter with high voltage gain and reduced voltage stresses," *IEEE Transactions on Power Electronics*, vol. 34, no. 3, pp. 2397–2404, 2019.

[24] R. Banupriya and R. Nagarajan, "Performance analysis of a relift Luo converter-derived dual-output DC to DC converter for microgrid applications," *International Journal of Photoenergy*, vol. 2022, Article ID 8093589, 19 pages, 2022.

[25] B. Faridpak, M. Farrokhifar, M. Nasiri, A. Alahyari, and N. Sadoogi, "Developing a super-lift Luo-converter with integration of buck converters for electric vehicle applications," *CSEE Journal of Power and Energy Systems*, vol. 7, no. 4, pp. 811–820, 2021.

[26] F. Ghasemi, M. R. Yazdani, and M. Delshad, "Step-up DC-DC switching converter with single switch and multi-outputs based on Luo topology," *IEEE Access*, vol. 10, pp. 16871–16882, 2022.

[27] S. Mahdizadeh, H. Gholizadeh, and S. A. Gorji, "A power converter based on the combination of Cuk and positive output super lift Lou converters: circuit analysis, simulation and experimental validation," *IEEE Access*, vol. 10, pp. 52899–52911, 2022.

[28] E. D. Aranda, S. P. Litrán, and M. B. F. Prieto, "Combination of interleaved single-input multiple-output DC-DC converters," *CSEE Journal of Power and Energy Systems*, vol. 8, no. 1, pp. 132–142, 2022.

[29] K. Suresh, C. Bharatiraja, N. Chellammal et al., "A multifunctional non-isolated dual input-dual output converter for electric vehicle applications," *IEEE Access*, vol. 9, pp. 64445–64460, 2021.

[30] V. F. Pires, A. Cordeiro, D. Foito, and J. F. A. Silva, "Dual output and high voltage gain DC-DC converter for PV and fuel cell generators connected to DC bipolar microgrids," *IEEE Access*, vol. 9, pp. 157124–157133, 2021.